AGU ADVANCING EARTH AND SPACE SCIENCES

Geophysical Research Letters

RESEARCH LETTER
10.1029/2026GL121719

Wind-Front Interactions Drive Intense Turbulence at the Oceanic Submesoscale

Hieu T. Pham[1], Sutanu Sarkar[1,2], Siddhant Kerhalkar[3,4], and Amit Tandon[3]

[1]Mechanical and Aerospace Engineering, University of California San Diego, La Jolla, CA, USA, [2]Scripps Institution of Oceanography, University of California San Diego, La Jolla, CA, USA, [3]School for Marine Science and Technology, University of Massachusetts Dartmouth, New Bedford, MA, USA, [4]School of Ocean and Earth Science and Technology, University of Hawai'i at Manoa, Honolulu, HI, USA

Key Points:

- Observations in a tropical cyclone wake reveal a marginally unstable shear layer, suggesting enhanced subsurface turbulence
- These large-eddy simulations of a tropical cyclone wake reveal enhanced turbulence by the downfront wind and, surprisingly, also the upfront wind
- Dissipation scaling at strong, narrow submesoscale fronts deviates from established theories derived for infinitely wide frontal regions

Supporting Information:

Supporting Information may be found in the online version of this article.

Correspondence to:

H. T. Pham,
h8pham@ucsd.edu

Citation:

Pham, H. T., Sarkar, S., Kerhalkar, S., & Tandon, A. (2026). Wind-front interactions drive intense turbulence at the oceanic submesoscale. *Geophysical Research Letters*, *53*, e2026GL121719. https://doi.org/10.1029/2026GL121719

Received 14 JAN 2026
Accepted 18 MAY 2026

Author Contributions:

Conceptualization: Hieu T. Pham, Sutanu Sarkar, Amit Tandon
Data curation: Hieu T. Pham, Siddhant Kerhalkar
Formal analysis: Hieu T. Pham
Funding acquisition: Sutanu Sarkar, Amit Tandon
Investigation: Hieu T. Pham, Sutanu Sarkar, Amit Tandon
Methodology: Hieu T. Pham, Sutanu Sarkar
Project administration: Sutanu Sarkar, Amit Tandon
Software: Hieu T. Pham
Supervision: Sutanu Sarkar

Abstract Observations of the cold wake of Cyclone Biparjoy in the Arabian Sea reveal an asymmetrical boundary layer structure across a dense water filament (DWF). This asymmetry arises from the interaction between monsoonal winds and uniquely strong frontal buoyancy gradients. Large-eddy simulations capture the observed contrast between the downfront wind and upfront wind sides of the DWF, which are respectively destabilized and stabilized by the Ekman buoyancy flux (B_{Ek}). Distinct patches of enhanced turbulence on both sides of the DWF indicate multiple triggering mechanisms. While the highest dissipation rates (ε) occur below the surface mixed layer at the downfront edge–with values exceeding B_{Ek}–dissipation on the upfront side is comparably large despite the nominally stabilizing effect of B_{Ek}. The frontal-averaged profile of ε on the downfront side deviates from established theories of front-wind interaction. These findings necessitate a re-evaluation of frontal turbulence dynamics and their representation in numerical parameterizations.

Plain Language Summary This study demonstrates how the interaction between surface winds and submesoscale fronts induces intense turbulence, potentially modulating thermal transport across the air-sea interface. Utilizing the exceptionally strong fronts observed at the edges of the wake of Cyclone Biparjoy, numerical simulations reveal large subsurface heat fluxes relative to the observed daily net heat input. These results highlight complex turbulent processes that are governed by wind, local lateral density gradients and their relative orientation. These processes contribute critically to upper-ocean evolution following extreme weather events.

1. Introduction

Submesoscale fronts and filaments are ubiquitous features of the upper ocean surface layer, acting as primary sites for surface convergence, downwelling, enhanced turbulent mixing, and the air–sea exchange of tracers, momentum, and energy (Mahadevan et al., 2020; McWilliams, 2021; Taylor & Thompson, 2023). Frontal turbulence is driven by multiscale 3D processes (Haney et al., 2012; Sarkar et al., 2016), yet their complex interactions with surface wind stress (τ) challenge the identification, quantification, and parameterization of the resulting mixing (D'Asaro et al., 2011; Hamlington et al., 2014; Thomas et al., 2013; Zheng et al., 2025). Furthermore, the interaction between vertical and horizontal turbulent processes within narrow submesoscale fronts–characterized by intense lateral buoyancy gradients ($|\nabla_h b|$)–differs significantly from the dynamics of weaker mesoscale fronts (Bodner et al., 2023; Chor et al., 2022; Sullivan & McWilliams, 2024). In this study, we employ large-eddy simulations (LES) motivated by observations of asymmetric evolution of mixed layer depths between the two sides of a dense water filament (DWF) with a strong horizontal buoyancy gradient to provide a new perspective on frontal mixing, uncovering regions of intense turbulence and elucidating the underlying physical mechanisms.

The cold wake of Cyclone Biparjoy in the Arabian Sea (summer 2023) exhibited a DWF characterized by exceptionally high lateral buoyancy gradients at its boundaries (Kerhalkar et al., 2025). The local values of $|\nabla_h b|$ can reach up to $270f^2$ where f is the Coriolis parameter. Under the influence of monsoonal winds, the DWF was subjected to stabilizing and destabilizing Ekman buoyancy fluxes by upfront and downfront winds, respectively, leading to an asymmetric structural evolution. This flux is defined as: $B_{Ek} = \frac{\vec{\tau}\times\hat{k}}{\rho_0 f}\cdot\nabla_h b$ where $\hat{k}$ is the vertical unit vector, and ρ_0 is the reference density. Based on turbulence parameterizations for symmetric instability (SI) under thermal wind balance (Thomas et al., 2013), the intense destabilizing B_{Ek} by the downfront wind likely induced enhanced turbulent production. Conversely, the stabilizing B_{Ek} induced by the upfront wind was expected to

Visualization: Hieu T. Pham, Siddhant Kerhalkar
Writing – original draft: Hieu T. Pham, Sutanu Sarkar
Writing – review & editing: Siddhant Kerhalkar, Amit Tandon

suppress mixed-layer turbulence. However, the absence of in situ turbulence measurements within the wake necessitates the use of high-resolution modeling to evaluate these theoretical predictions.

These observations motivate us to perform LES of a modeled DWF with such uniquely strong $|\nabla_h b|$ to examine its evolution under an applied wind stress. More broadly, this study investigates the role of Ekman transport as a primary driver of frontal turbulence in the previously unexplored regime of strong, narrow fronts. The remainder of this paper is organized as follows: Section 2 details the relevant observational data and the physical motivations that necessitate the numerical approach; Section 3 describes the LES configuration and model parameters; Section 4 contrasts the asymmetrical evolution of turbulence at the DWF boundaries; Section 5 elucidates the physical mechanisms triggering this asymmetry; Section 6 presents a turbulent kinetic energy (TKE) budget analysis to assess the scaling laws that govern frontal turbulence; and Section 7 discusses the broader implications of these findings and provides concluding remarks.

2. Observation of Dense Water Filament in the Cyclone Wake

The passage of Cyclone Biparjoy along the west coast of India left a cold, saline DWF characterized by a uniquely strong $|\nabla_h b|$ at its edges (Figure 1a). Underway CTD measurements, with a cross-front horizontal resolution of approximately between 1.2 and 1.7 km, indicate localized values of $|\nabla_h b|/f^2$ reaching up to 270 (Kerhalkar et al., 2025). The balanced Rossby number ($Ro_b = H|\nabla_h b|/f^2 L$ where H and L denote the vertical and lateral spatial extent of the submesoscale fronts) reaches values up to 5.3 when estimated using the smooth (over 4-km horizontal distance) density profiles (Figure S2 in Supporting Information S1). Under a northward wind stress of $\tau \approx 0.1\ \mathrm{N\,m^{-2}}$, the upfront (western) and downfront (eastern) edges of the DWF were subjected to intense B_{Ek}. The equivalent heat flux, defined as $J_{Ek} = \rho_0 c_p B_{Ek}/\alpha g$, was $\mathcal{O}(500\ \mathrm{W\,m^{-2}})$ in magnitude–significant relative to the daily net surface heat flux $(Q_{net} \approx 150\ \mathrm{W\,m^{-2}})$.

Ship-based ADCP data reveal counter-flowing currents on either side of the DWF. Meridional velocities in the upper 70 m indicate southward flows near the western edge and northward flows near the eastern edge (see Figures 3c and 3d in Kerhalkar et al. (2025)). This flow direction is qualitatively consistent with thermal wind balance, where southward (northward) currents correspond to negative (positive) $\nabla_h b$. However, the coarse resolution of the ADCP data precludes a precise quantitative verification of thermal wind balance. Profiles of buoyancy frequency (N^2) and squared shear (Sh^2) reveal a marginally unstable layer between 30 and 50 m depth, with gradient Richardson numbers $(Ri_g = N^2/Sh^2)$ ranging between 0.25 and 1 (Figure 1b) (see Thorpe and Liu (2009)). Such marginal values in frontal regions suggest the potential for enhanced turbulent mixing driven by SI (Hoskins & Bretherton, 1972; Thomas & Taylor, 2010).

The surveyed density field reveals a distinct asymmetry in the frontal structure (Figure 1a). The MLD is approximately 12 m deeper on the downfront wind side despite the peak $|\nabla_h b|$ values at the two edges being comparable (Figures S2b and S2d in Supporting Information S1). Turbulence was not measured during the survey. While positive (destabilizing) B_{Ek} on the downfront wind side and negative (stabilizing) B_{Ek} on the upfront wind side inherently drive MLD asymmetry, how enhanced downfront turbulence reinforces $|\nabla_h b|$ remains unresolved.

To elucidate the asymmetric interaction between wind forcing and frontal dynamics, including frontal turbulence, we performed LES constrained by background flow and wind forcing consistent with observational data. The resulting LES density field (Figure 1c) shows similar MLD asymmetry, that is, shallower MLD on the upfront wind side. Notably, the LES also captures the enhanced $|\nabla_h b|$ on the downfront wind side. The turbulent dissipation rate (ε) indicates enhanced turbulence at not only the downfront wind side but, *surprisingly,* also on the upfront wind side of the DWF relative to regions with no front (Figure 1d). In the following sections, we analyze the DWF evolution to explicate the role of frontal turbulence.

3. An LES Model of the Dense Water Filament

Large-eddy simulations of a cold, saline DWF at 12°N were performed with the initial configuration (Figure S1 in Supporting Information S1) consisting of two partially-compensated, salinity-controlled submesoscale fronts separated by 13 km in the cross-front (y) direction. Each front has a width $L = 3$ km and depth $H = 70$ m, initialized in thermal wind balance with along-front jets (u). Initial T and S profiles define a mixed layer

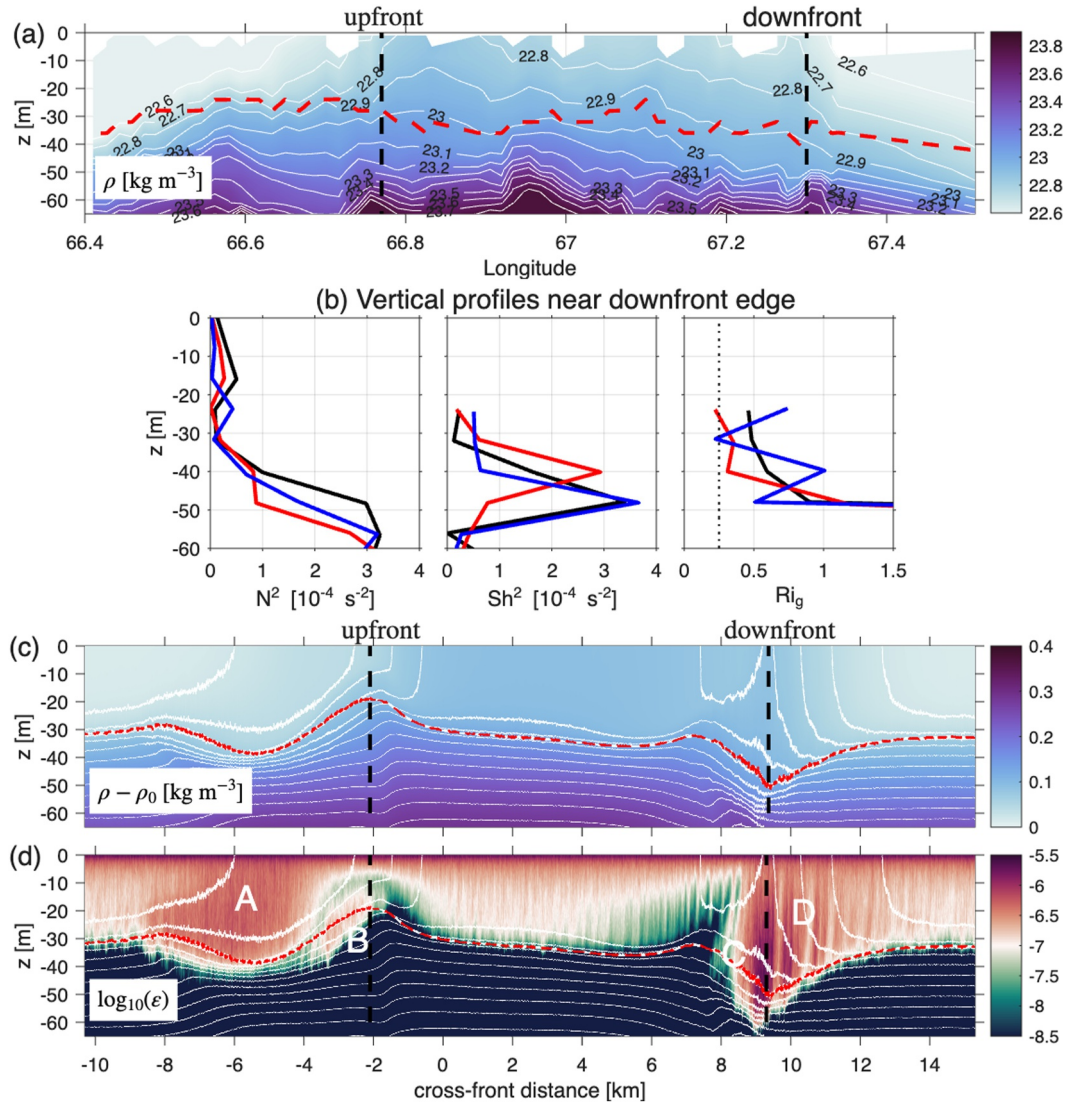

Figure 1. Observations of the cold wake behind Cyclone Biparjoy (a, b) and results from the large-eddy simulations (LES) model of a dense water filament (DWF) in the F4 simulation (c, d). Cross-front density field in (a) illustrates the saline cold DWF observed in the wake. Profiles of stratification N^2, squared shear Sh^2 and gradient Richardson number Ri_g in (b) indicate a subsurface marginally-unstable shear layer near the downfront edge. The LES along-front averaged density field (c) at $t = 17.2$ hr shows similarity with observations (a). The LES along-front averaged dissipation rate (ε) field (d) reveals asymmetric enhancement of turbulence patches at the DWF edges as indicated by markers A through D. In panels (a, c, d), white solid lines are isopycnals, red dashed lines denote the mixed-layer depth, and black dashed lines mark the DWF edges where $|\nabla_h b|$ peaks. The dotted black line in the Ri_g panel marks the critical value for shear instabilities.

($h = 20$ m) overlying a constant-stratification interior. A constant wind stress $\left(\tau = 0.1\,\mathrm{N\,m^{-2}}\right)$ is applied in the negative x-direction (pointing into the page), driving a rightward Ekman transport ($+y$ direction). Consequently, the front at $y = -6.5$ km experiences a negative B_{Ek} (upfront wind, stabilizing), while the front at $y = 6.5$ km experiences a positive B_{Ek} (downfront wind, destabilizing).

We varied $\nabla_h b$ and N^2 in 6 simulations (namely, F1–F6) to explore a range of balanced Richardson numbers $\left(Ri_b = N^2 f^2/(\nabla_h b)^2\right)$ between 0.44 and 2 and balanced Rossby number between 4.3 and 11.4 (Table S1 in Supporting Information S1). In addition to unforced centrifugal-symmetric instabilities which can lead to turbulence in this range of Ri_b and Ro_b (Chor et al., 2022; Haine & Marshall, 1998; Thomas et al., 2013), ageostrophic secondary circulations (ASC) can enhance mixed-layer turbulence via lateral processes in fronts with large $|\nabla_h b|$ (Pham & Sarkar, 2018).

ML turbulence characteristics vary across the DWF. Outside the frontal regions, the dissipation rate (ε) at mid-mixed-layer depth ($h/2$) for a purely wind-driven Ekman layer scales as $\varepsilon = 2u_*^3/h$, where u_* is the friction velocity (Belcher et al., 2012). On the downfront wind side, studies of forced SI in infinitely wide frontal regions suggest $\varepsilon \propto B_{Ek}$ (Thomas et al., 2013; Thomas & Taylor, 2010); however, this scaling requires verification for the finite-width fronts considered here. Furthermore, the scaling of ε under the stabilizing B_{Ek} by the upfront wind in finite-width fronts (i.e., patches A and B in Figure 1d) side remains poorly understood.

Table S1 in Supporting Information S1 details the LES parameters, including $|\nabla_h b|/f^2$, B_{Ek}, Ri_b and Ro_b. Under thermal wind balance, increasing $|\nabla_h b|$ strengthens the geostrophic jet velocity and shear. Thus, destabilization or stabilization in the wind/front system (as measured by B_{Ek}) occurs over fast timescales (hours) due to large $|\nabla_h b|$ and geostrophic shear. Each simulation spans 18 hr, sufficient to capture the rapid DWF evolution.

The non-hydrostatic Navier-Stokes equations, under the Boussinesq approximation, were solved using a horizontally periodic domain of 360 × 30,722.5 × 160 m in the along-front (x), cross-front (y) and vertical (z) directions, respectively. The grid employs 288 × 24,578 × 320 points (about 2.3 billion), with a uniform horizontal resolution of 1.25 m. Vertically, $\Delta z = 0.3$ m above 70 m, with 3% stretching below. The LES computational domain in the along-front direction is too short to capture MLI, but is sufficient to capture turbulent wind-front interaction dynamics as will be shown. A 40-m sponge layer at the bottom prevents spurious internal wave reflections. Statistics were obtained using Reynolds decomposition, angle brackets denoting along-front averages.

4. Enhanced Turbulence Across the DWF

Four distinct regions of enhanced dissipation–patches A and B on the upfront wind side and C and D on the downfront wind side (Figure 1d)–exhibit values at least an order of magnitude greater than those found outside the frontal zones at the same depth. In contrast to the blob-like ε in patches A, B, and C, patch D is characterized by multiple thin bands of elevated dissipation spanning the region to the right of the downfront wind edge. The bands become more prominent as $|\nabla_h b|$ increases in cases F5 and F6 as shown later in Figure 4a. While A and D are primarily confined within the MLD, B extends below the MLD. Patch C, situated at the downfront edge where $|\nabla_h b|$ peaks, exhibits the highest values of ε and penetrates deepest into the pycnocline. In the LES analysis, the MLD is defined by a density of $0.04\,\mathrm{kg\,m^{-3}}$ increase relative to surface values, a threshold that consistently captures the wind-driven MLD across all cases. The shallowest MLD occurs near the upfront wind edge, where negative B_{Ek} facilitates frontal slumping, whereas the MLD at the downfront wind edge is significantly deeper, consistent with observations.

The turbulent patches emerge as the developing surface Ekman layer disrupts the initial thermal wind balance. Ekman transport advects the DWF rightward (Figures 2a–2c); specifically, after 17.2 hr, the upfront and downfront wind edges shift from their initial positions ($y = -6.5$ km and $+6.5$ km) to $y = -2.1$ km and $y = 9.4$ km, respectively (Figure 2a). This lateral advection induces a differential horizontal displacement of the frontal jets, where the upper portion undergoes a positive y-displacement while the lower portion remains relatively static ($\langle u \rangle$ in Figure 2b).

In 2D frontal flows with no wind forcing, the ASC is characterized by counter-flowing surface and subsurface limbs (Thompson, 2000). Under wind forcing, however, the Ekman transport and the surface component of the ASC align on the upfront wind side but oppose one another on the downfront wind side (see Figure S3f in Supporting Information S1). This alignment results in higher cross-front velocities (v) on the upfront side (Figure 2c). Due to the stronger cross-front component of the Ekman current relative to the ASC, net v remains positive throughout the DWF domain (Figures S3a, S3d, and S3f in Supporting Information S1).

The upper and lower limbs of the ASC drive the turbulence in patches A and B, respectively (see Figure S3f in Supporting Information S1). These patches correlate with layers of elevated squared shear and $Ri_g < 0.25$ (Figures 2d and 2e). Patches C and D display relatively weak shear throughout the majority of the water column due to intense mixing, with elevated shear restricted to the base of the patch within the pycnocline. Analysis of TKE budgets indicates that the turbulence in the four patches is driven by shear instabilities (Figure S4 in Supporting Information S1).

The strongest dissipation in patch C is facilitated by strengthened Sh^2 and reduced N^2 by the downfront wind condition. Although Ekman transport reduces stratification at the downfront wind edge by advecting dense water

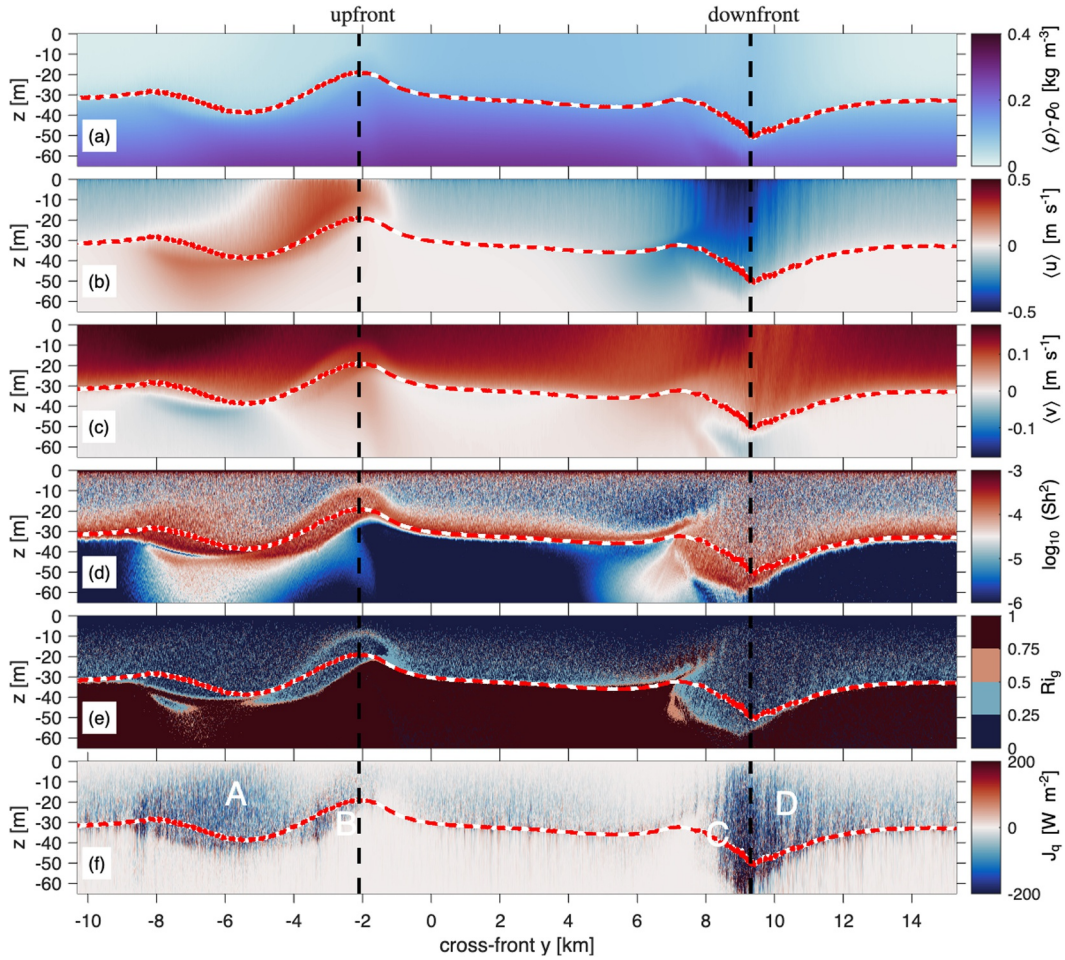

Figure 2. Asymmetric evolution of the dense water filament (DWF) in case F4 at time t = 17.2 hr: (a) density deviation $\langle\rho\rangle$–$\langle\rho_0\rangle$, (b) along-front velocity $\langle u\rangle$, (c) cross-front velocity $\langle v\rangle$, (d) squared shear Sh^2, (e) gradient Richardson number Ri_g, and (f) turbulent heat flux J_q. Vertical dashed lines mark the DWF edges where $|\nabla_h b|$ peaks. Red dashed lines denote the mixed-layer depth. The fields are along-front averages.

over lighter water, explicit convective instabilities are not observed in patch C (see Figure S4 in Supporting Information S1). Instead, turbulence is primarily shear-driven, yielding a negative turbulent buoyancy flux (B). Turbulence in patch C supports a substantial subsurface heat flux (J_q) of up to $-230\,\mathrm{Wm}^{-2}$ in case F4 ($-600\,\mathrm{Wm}^{-2}$ in case F6), significantly exceeding the daily surface heat flux (Figure 2f).

5. Shear-Driven Mixing Is Enhanced by Lateral Advection

5.1. Advection on the Upfront Wind Side

Lateral advection induces elevated shear in patches A and B, as evidenced by the evolution of velocity and shear components between time t = 5.1 and 13.4 hr (panels a–d in Box A of Figure 3). Ekman transport ($\langle v\rangle$ in panel b at t = 5.1 hr) distorts the frontal jet ($\langle u\rangle$ in panel a at t = 13.4 hr) by displacing the upper portion in the positive y-direction over the quiescent pycnocline. Prior to this displacement, $\partial\langle u\rangle/\partial z$ in the region surrounding $y = -6.5$ km reflects the positive shear of the initial geostrophic jet (panel c at t = 5.1 hr). The subsequent distortion of the jet results in enhanced negative shear ($\partial\langle u\rangle/\partial z$) within patch A and enhanced positive shear ($\partial\langle u\rangle/\partial z$) within patch B (panel c at t = 13.4 hr).

The large negative $\partial\langle u\rangle/\partial z$ in patch A is driven by the vertical entrainment of negative wind-driven momentum into the positively directed jet. Conversely, the enhanced positive $\partial\langle u\rangle/\partial z$ in patch B results from the lateral advection of the upper frontal jet over the zero-velocity pycnocline. A thin layer characterized by $Ri_g > 0.25$

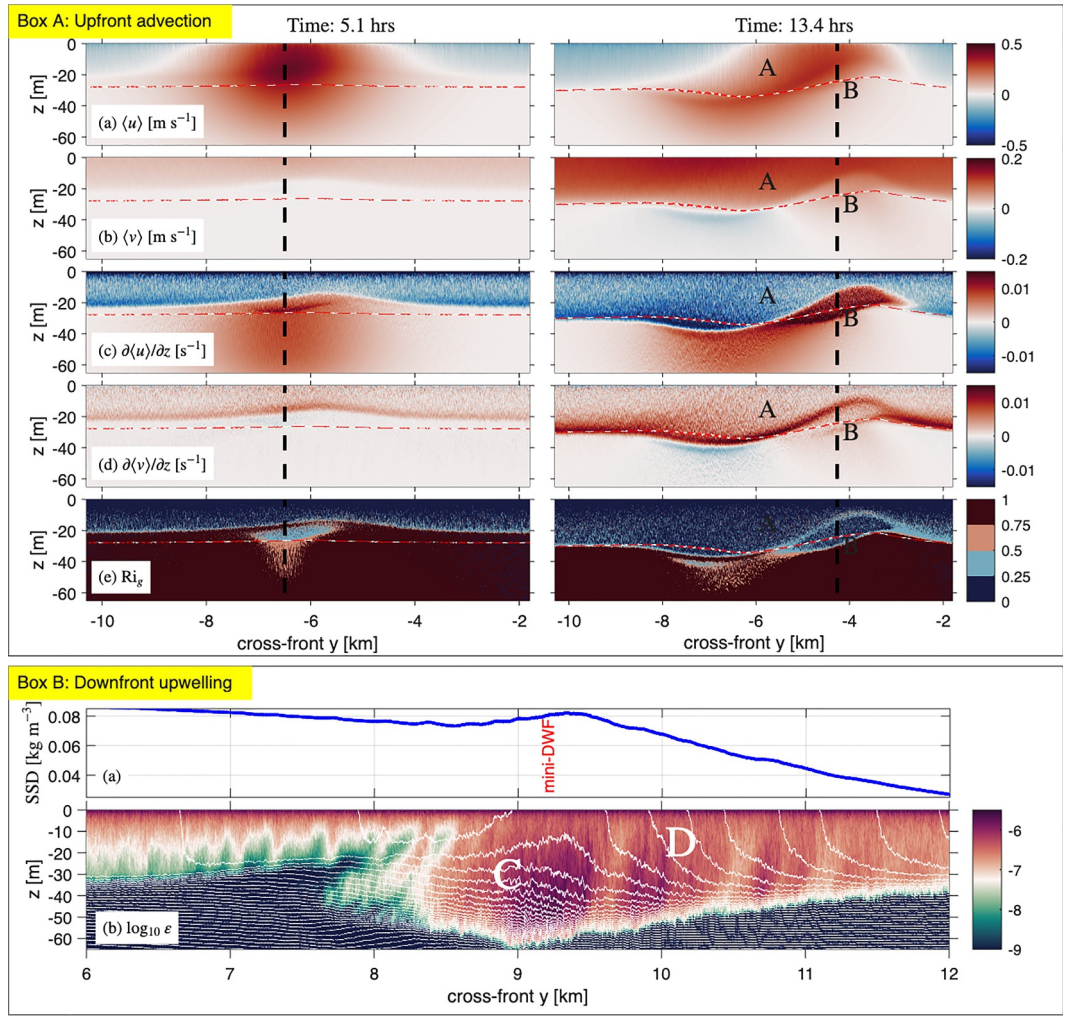

Figure 3. Box A shows shear enhancement by cross-front Ekman transport at the upfront wind edge in case F4: (a) along-front velocity $\langle u \rangle$, (b) cross-front velocity $\langle v \rangle$, (c) along-front vertical shear $\partial\langle u \rangle/\partial z$, (d) cross-front vertical shear $\partial\langle v \rangle/\partial z$, and (e) gradient Richardson number Ri_g. Vertical dashed lines mark the local peak of $\langle u \rangle$ at surface and red dashed lines denote the mixed-layer depth. Box B shows the upwelling of dense water and the formation of a mini-DWF in patch C at $t = 17.2$ hr for case F4: (a) sea surface density deviation from ρ_0 and (b) ε. White solid lines denote isopycnals.

separates the surface Ekman layer from patch B (panel e at $t = 13.4$ hr). Thus, the subsurface enhanced turbulence of patch B is decoupled from direct wind-driven entrainment.

Ekman transport is fundamental to the turbulence enhancement in patches A and B, both through the dislocation of the frontal jet and the generation of associated cross-front shear $\partial\langle v \rangle/\partial z$ (panels b and d at time = 13.4 hr in Box A of Figure 3). In patch A, the magnitudes of the two shear components are comparable, whereas $\partial\langle u \rangle/\partial z$ dominates in patch B. Specifically, patch B exhibits thin layers of intensified $\partial\langle v \rangle/\partial z$ at its upper and lower boundaries, while the interior of the patch is characterized by broadly elevated positive $\partial\langle u \rangle/\partial z$.

5.2. Upwelling by Turbulence on the Downfront Wind Side

Mixing within patch C is intensified by the formation of a "mini-DWF" at the downfront edge. Sea surface density exhibits a localized density maximum where surface water is denser than its immediate surroundings (panel a in Box B of Figure 3). This feature is driven by shear instabilities within patch C that efficiently transport dense water from the pycnocline to the surface. This upward transport results in the doming of isopycnals–forming the "mini-DWF"–at the precise location where ε is most intense (panel b in Box B of Figure 3).

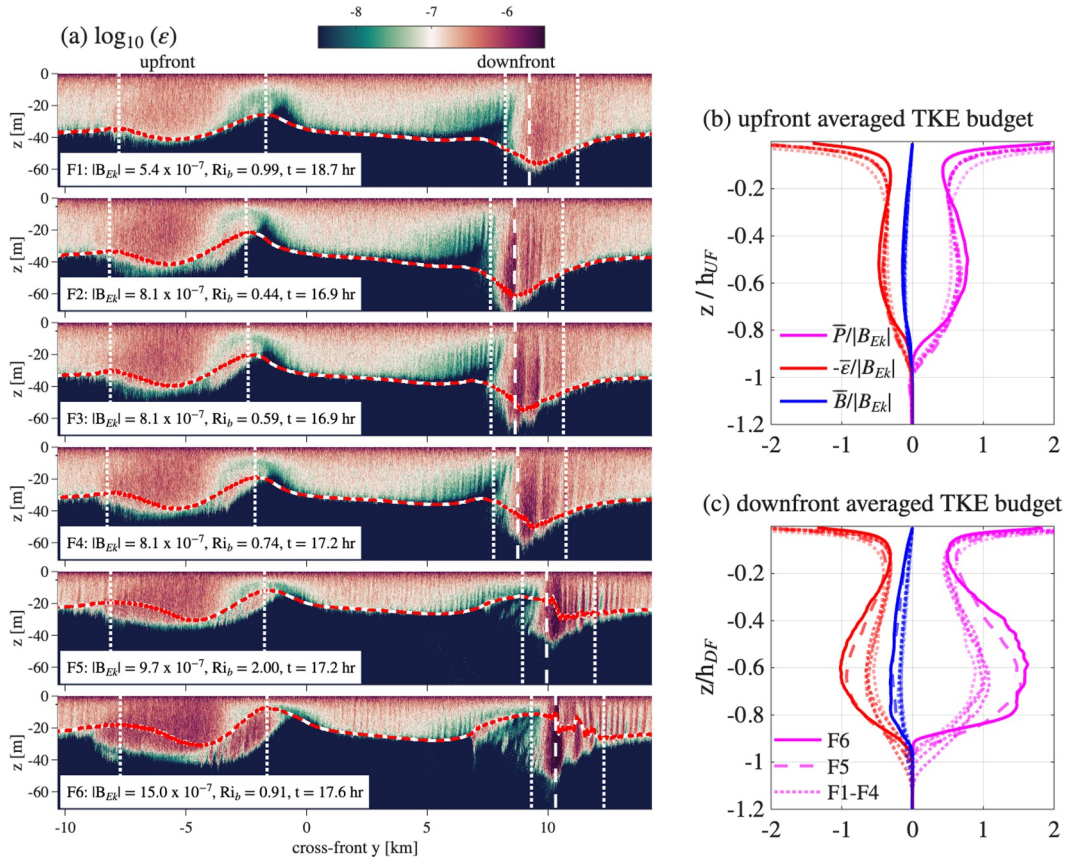

Figure 4. Scaling of frontal dissipation: (a) ϵ in all large-eddy simulations cases; (b, c) frontal averaged profiles of turbulent production $\bar{P}$ (magenta), dissipation $\bar{\epsilon}$ (red) and buoyancy flux $\bar{B}$ (blue) on the upfront and downfront sides, respectively. In panels (b and c), colors indicate different terms in the turbulent kinetic energy budget while line types denote different cases. Profiles in cases F5 and F6 are marked with solid and dashed lines, respectively, while dotted lines are used for cases F1 to F4. The vertical axes in panels (b and c) are scaled by h_{UF} and h_{DF}, the greatest depths where the cross-front averaged $\epsilon > 10^{-8}\ \mathrm{m^2\ s^{-3}}$ on the upfront and downfront wind sides, respectively. The budget terms are normalized by the initial B_{Ek} values. Dotted white lines in (a) mark the regions (left pair for upfront wind and right pair for downfront wind) used for frontal averaging. Dashed white lines mark location of strongest $|\nabla_h b|$ on the downfront wind side.

The mini-DWF represents a significant turbulence-driven frontal feature where vertical and horizontal processes mutually reinforce one another. Vertical mixing facilitates the shoaling of dense water from depth, which locally increases $|\nabla_h b|$. The stronger are the vertical mixing and upward transport, the larger are the lateral density gradient and B_{Ek}. This, in turn, enhances destabilization and further stimulates vertical mixing (as seen in cases F5 and F6). This positive feedback loop between frontal turbulence and the lateral buoyancy gradient explains why the ship's throughflow system shows significantly high values of $|\nabla_h b|$ near the downfront edge despite the deep MLD (Figure S2d in Supporting Information S1). The feedback mechanism suggests frontogenesis can be strengthened by vertical turbulent diffusivity (Crowe & Taylor, 2018), and convective turbulence has been found to strengthen horizontal convergence and increase coherent submesosale vertical downwelling (Verma et al., 2022). Dauhajre et al. (2025) suggested frontal sharpening when the parameter Ro^2/Ek approximately exceeds 50, a criterion that is met here.

The intensification of local $|\nabla_h b|$ is further supported by the convergence of lighter fluid on either side of the mini-DWF. The previously shown $\langle v \rangle$ field in Figure 2c indicates a narrow region of elevated negative $\partial\langle v \rangle/\partial y$ at the downfront wind edge. While this near-surface compressive strain increases the local $|\nabla_h b|$, it cannot account for the increase in surface density itself. In an arrested DWF, the convergence of lighter fluid typically induces downwelling (Sullivan & McWilliams, 2018, 2024); however, in the present study, the upward transport of dense water by subsurface shear instabilities dominates, resulting in net upwelling.

Although less intense than in patch C, patch D exhibits vertical bands of elevated ϵ with a horizontal spacing of approximately 200 m that cross the sloping isopycnals (panel b in Box B of Figure 3). The bands are more prominent in cases F5 and F6 (see Figure 4a). These bands manifest shear instabilities developing in the along-front direction rather than centrifugal-symmetric instabilities (see TKE budgets in Figure S4 in Supporting Information S1). While SI typically aligns with sloping isopycnals in regions where $0.25 < Ri_g < 0.95$ (Arobone & Sarkar, 2015; Taylor & Ferrari, 2009, 2010), the instabilities in patch D occur where $Ri_g < 0.25$ (recall Figure 2e).

6. Scaling of Frontal Mixing

Turbulent patches A, C and D occur across all six simulated cases, persisting over a broad parameter space of $|\nabla_h b|$ and Ri_b, including case F5 where $Ri_b = 2$ (Figure 4a). Relative to the other cases, patch B turbulence is not as strong in case F1 where $|\nabla_h b|$ is the weakest. Increasing B_{Ek} intensifies turbulence in all four patches (e.g., compare F6 to F1). Conversely, at the same value of B_{Ek}, increasing Ri_b through higher N^2 leads to a moderate reduction in vertical extent (F4 to F2). The mini-DWF intensifies in cases F5 and F6, which are characterized by both large B_{Ek} and Ri_b. In F5 and F6, upwelling effectively shoals the MLD at the downfront wind edge, in contrast to cases F1 - F4, where the MLD penetrates deeper into the pycnocline.

Frontal-averaged profiles of turbulent production $(\bar{P})$, dissipation $(\bar{\varepsilon})$, and buoyancy flux $(\bar{B})$ indicate downfront mixing is significantly more vigorous than at the upfront side (Figures 4b and 4c). Thus, the net turbulence in patches C and D is stronger than the combination of patches A and B. When scaled by the initial B_{Ek} values, the vertical profiles of $\bar{P}$, $\bar{\varepsilon}$, and $\bar{B}$ on the upfront side collapse across all simulated cases (Figure 4b). In contrast, no such collapse is observed on the downfront side (Figure 4c). The subsurface peak of $\bar{P}$ in cases F5 and F6 significantly exceeds B_{Ek}. These results demonstrate that turbulence scaling must account for the positive feedback mechanism that intensifies the local $|\nabla_h b|$.

7. Discussion and Conclusions

Using LES of a model DWF, we demonstrate how lateral advection–driven by Ekman transport and 2D ASC across strong submesoscale fronts–leads to the observed asymmetric density structure, MLD, and $|\nabla_h b|$ documented in the wake of Cyclone Biparjoy. On the side with upfront wind, lateral advection distorts the frontal jets, enhances vertical shear, and reduces the gradient Richardson number $Ri_g < 0.25$. These processes trigger shear instabilities that manifest as distinct turbulent patches A and B (Box A of Figure 3). On the side with downfront wind, the shear instabilities (patch C) are intensified by B_{Ek} -driven destabilization and the upwelling of dense water, which forms a "mini-DWF" (Box B of Figure 3) that in turn locally intensifies B_{Ek}. Thus, there is a positive feedback loop between vertical mixing and $|\nabla_h b|$ at the mini-DWF. We note that the submesoscale fronts in the present study extend deeper than the initial mixed layer and have relatively high Ro number. The importance of the turbulence mechanisms identified here in other situations with shallower fronts and with lower Ro requires further study.

While observations of the Cyclone Biparjoy wake indicate the influence of lateral advection on vertical shear at the upfront edge (Figure S5 in Supporting Information S1), our simulations demonstrate that such advection additionally enhances turbulent mixing on both flanks of a DWF. The post-cyclone wake was observed to recover much faster than 1-D mixing model predictions, highlighting the contribution of submesoscale processes to the quick recovery (Kerhalkar et al., 2025). Here, we present direct evidence of submesoscale turbulence in a similar model wake noting the absence of MLI in our model setup.

Turbulence enhancement by the upfront wind (stabilizing B_{Ek}) is counter-intuitive in view of the expectation of restratification. The distortion of the frontal jet by Ekman momentum transport triggers subsurface mixing in patch B. Furthermore, the intense mixing in the patch C by downfront wind produces a subsurface turbulent heat flux exceeding the observed daily surface heat flux (especially in cases F5 and F6) representing a potential mechanism for SST cooling from below.

A TKE budget analysis reveals that at strong submesoscale fronts under destabilizing wind conditions, frontal-averaged turbulent production $(\bar{P})$ can exceed B_{Ek} (Figure 4d). This result contrasts with previous numerical studies of infinitely wide frontal regions favoring SI (Taylor & Ferrari, 2010; Thomas et al., 2013; Thomas &

Taylor, 2010; Zheng et al., 2025). In those idealized "Eady-type" configurations, $\nabla_h b$ and thermal wind shear ($\partial u/\partial z$) are held constant, and geostrophic shear production typically peaks at the surface before decreasing monotonically with depth. In contrast, the finite-width fronts studied here possess Rossby numbers Ro (based on frontal width and the frontal jet velocity) greater than unity, and the value of $\nabla_h b$ and $\partial u/\partial z$ are free to evolve dynamically. Here, turbulent production (P) shows enhanced values below the MLD. Our results indicate that in high-$|\nabla_h b|$ regimes with large $B_{Ek}h/u_*^3$ (Table S1 in Supporting Information S1), shear production by a wind-distorted frontal jet contributes more significantly to the TKE budget than wind forcing alone, particularly at depth. Consequently, parameterizations of frontal mixing based exclusively on SI (e.g., Dong et al., 2024) should be revisited for the present regime of submesoscale fronts where lateral advection and jet distortion may emerge as the primary drivers of frontal turbulence.

Conflict of Interest

The authors declare no conflicts of interest relevant to this study.

Availability Statement

ADCP and uCTD data from the survey are embargoed until 2029 under an agreement between the U.S. and India. This timeframe ensures that students and postdoctoral researchers supported by the project have sufficient time to publish observation-based results. The LES data are available in Pham (2026).

Acknowledgments
The authors gratefully acknowledge the support of the US Office of Naval Research for the EKAMSAT-ASTraL Department Research Initiative. H. Pham and S. Sarkar received support from N00014-23-1-2481, S. Kerhalkar and A. Tandon from N00014-23-1-2054. S. Kerhalkar was additionally supported under Grant N00014-24-1-2570 (PI: Hyodae Seo). We thank Ankitha Kannad and Janet Sprintall for providing the uCTD measurements. Constructive comments from two anonymous reviewers greatly improve the manuscript.

References

Arobone, E., & Sarkar, S. (2015). Effects of three-dimensionality on instability and turbulence in a frontal zone. *Journal of Fluid Mechanics*, *784*, 252–273. https://doi.org/10.1017/jfm.2015.564

Belcher, S. E., Grant, A. L. M., Hanley, K. E., Fox-Kemper, B., Van Roekel, L., Sullivan, P. P., et al. (2012). A global perspective on Langmuir turbulence in the ocean surface boundary layer. *Geophysical Research Letters*, *39*(18). https://doi.org/10.1029/2012GL052932

Bodner, A. S., Fox-Kemper, B., Johnson, L., Roekel, L. P. V., McWilliams, J. C., Sullivan, P. P., et al. (2023). Modifying the mixed layer eddy parameterization to include frontogenesis arrest by boundary layer turbulence. *Journal of Physical Oceanography*, *53*(1), 323–339. https://doi.org/10.1175/JPO-D-21-0297.1

Chor, T., Wenegrat, J. O., & Taylor, J. (2022). Insights into the mixing efficiency of submesoscale centrifugal–symmetric instabilities. *Journal of Physical Oceanography*, *52*(10), 2273–2287. https://doi.org/10.1175/JPO-D-21-0259.1

Crowe, M. N., & Taylor, J. R. (2018). The evolution of a front in turbulent thermal wind balance. Part 1. Theory. *Journal of Fluid Mechanics*, *850*, 179–211. https://doi.org/10.1017/jfm.2018.448

D'Asaro, E. A., Lee, C. M., Rainville, L., Harcourt, R. R., & Thomas, L. N. (2011). Enhanced turbulence and energy dissipation at ocean fronts. *Science*, *322*(6027), 318–322. https://doi.org/10.1126/science.1201515

Dauhajre, D. P., Srinivasan, K., Molemaker, M. J., Gula, J., Hypolite, D., McWilliams, J. C., et al. (2025). Vertical mixing can both induce and inhibit submesoscale frontogenesis. *Journal of Physical Oceanography*, *55*(9), 1409–1433. https://doi.org/10.1175/JPO-D-24-0148.1

Dong, J., Fox-Kemper, B., Wenegrat, J. O., Bodner, A. S., Yu, X., Belcher, S., & Dong, C. (2024). Submesoscales are a significant turbulence source in global ocean surface boundary layer. *Nature Communications*, *15*(1), 9566. https://doi.org/10.1038/s41467-024-53959-y

Haine, T. W. N., & Marshall, J. (1998). Gravitational, symmetric and baroclinic instability of the ocean mixed layer. *Journal of Physical Oceanography*, *28*(4), 634–658. https://doi.org/10.1175/1520-0485(1998)028<0634:gsabio>2.0.co;2

Hamlington, P. E., Van Roekel, L. P., Fox-Kemper, B., Julien, K., & Chini, G. P. (2014). Langmuir-submesoscale interactions: Descriptive analysis of multiscale frontal spindown simulations. *Journal of Physical Oceanography*, *44*(9), 2249–2272. https://doi.org/10.1175/JPO-D-13-0139.1

Haney, S., Bachman, S., Cooper, B., Kupper, S., McCaffrey, K., Van Roekel, L., et al. (2012). Hurricane wake restratification rates of one-two- and three-dimensional processes. *Journal of Marine Research*, *70*(6), 824–850. https://doi.org/10.1357/002224012806770937

Hoskins, B. J., & Bretherton, F. P. (1972). Atmospheric frontogenesis models: Mathematical formulation and solution. *Journal of the Atmospheric Sciences*, *29*, 11–37. https://doi.org/10.1175/1520-0469(1972)029<0011:AFMMFA>2.0.CO;2

Kerhalkar, S., Kannad, A., Kinsella, A., Tandon, A., Sprintall, J., & Lee, C. M. (2025). Monsoon-frontal interactions drive cyclone biparjoy's wake recovery in the Arabian Sea. *Geophysical Research Letters*, *52*(4), e2024GL112413. https://doi.org/10.1029/2024GL112413

Mahadevan, A., Pascual, A., Rudnick, D. L., Ruiz, S., Tintoré, J., & D'Asaro, E. A. (2020). Coherent pathways for vertical transport from the surface ocean to interior. *Bulletin of the American Meteorological Society*, *101*(11), 1–21. https://doi.org/10.1175/BAMS-D-19-0305.1

McWilliams, J. C. (2021). Oceanic frontogenesis. *Annual Review of Marine Science*, *13*(1), 227–253. https://doi.org/10.1146/annurev-marine-032320-120725

Pham, H. T. (2026). Data and software for "wind-front interactions drive intense turbulence at the oceanic submesoscale" [Dataset]. *Zenodo*. https://doi.org/10.5281/zenodo.18182770

Pham, H. T., & Sarkar, S. (2018). Ageostrophic secondary circulation at a submesoscale front and the formation of gravity currents. *Journal of Physical Oceanography*, *48*(10), 2507–2529. https://doi.org/10.1175/JPO-D-17-0271.1

Sarkar, S., Pham, H. T., Ramachandran, S., Nash, J. D., Tandon, A., Buckley, J., et al. (2016). The interplay between submesoscale instabilities and turbulence in the surface layer of the Bay of Bengal. *Oceanography*, *29*(2), 146–157. https://doi.org/10.5670/oceanog.2016.47

Sullivan, P. P., & McWilliams, J. C. (2018). Frontogenesis and frontal arrest of a dense filament in the oceanic surface boundary layer. *Journal of Fluid Mechanics*, *837*, 341–380. https://doi.org/10.1017/jfm.2017.833

Sullivan, P. P., & McWilliams, J. C. (2024). Oceanic frontal turbulence. *Journal of Physical Oceanography*, *54*(2), 333–358. https://doi.org/10.1175/JPO-D-23-0033.1

Taylor, J. R., & Ferrari, R. (2009). On the equilibration of a symmetrically unstable front via a secondary shear instability. *Journal of Fluid Mechanics*, *622*, 103–113. https://doi.org/10.1017/S0022112008005272

Taylor, J. R., & Ferrari, R. (2010). Buoyancy and wind-driven convection at mixed layer density fronts. *Journal of Physical Oceanography*, *40*(6), 1222–1242. https://doi.org/10.1175/2010JPO4365.1

Taylor, J. R., & Thompson, A. F. (2023). Submesoscale dynamics in the upper ocean. *Annual Review of Fluid Mechanics*, *55*(1), 103–127. https://doi.org/10.1146/annurev-fluid-031422-095147

Thomas, L. N., & Taylor, J. R. (2010). Reduction of the usable wind-work on the general circulation by forced symmetric instability. *Geophysical Research Letters*, *37*(18), L18606. https://doi.org/10.1029/2010gl044680

Thomas, L. N., Taylor, J. R., Ferrari, R., & Joyce, T. M. (2013). Symmetric instability in the Gulf Stream. *Deep-Sea Research II*, *91*, 96–110. https://doi.org/10.1016/j.dsr2.2013.02.025

Thompson, L. (2000). Ekman layers and two-dimensional frontogenesis in the upper ocean. *Journal of Geophysical Research*, *105*(C3), 6437–6451. https://doi.org/10.1029/1999jc900336

Thorpe, S., & Liu, Z. (2009). Marginal instability? *Journal of Physical Oceanography*, *39*(9), 2373–2381. https://doi.org/10.1175/2009jpo4153.1

Verma, V., Pham, H. T., & Sarkar, S. (2022). Interaction between upper-ocean submesoscale currents and convective turbulence. *Journal of Physical Oceanography*, *52*(3), 437–458. https://doi.org/10.1175/JPO-D-21-0148.1

Zheng, Z., Wenegrat, J. O., Fox-Kemper, B., & Brett, G. J. (2025). Wind-catalyzed energy exchanges between fronts and boundary layer turbulence. *Journal of Physical Oceanography*, *55*(9), 1591–1606. https://doi.org/10.1175/JPO-D-24-0243.1